Current-voltage response for unipolar funnel-shaped nanochannel diodes

Yoav Green[*]

Harvard T. H. Chan School of Public Health, Boston, Massachusetts 02115, USA

Permselective nanochannels can rectify the electric current transported through them similar to solid-state diodes. The rectification is due to symmetry breaking related to distribution of the nanochannels' surface charge as well as the geometry. Thus far, most of the works related to the asymmetric current response have been primarily experimental. Here, we theoretically model a funnel-shaped nanochannel with a nonhomogeneous surface charge from which we derive a current-voltage relation (*I-V*). If the effects of the adjacent microchannels are ignored, the *I-V* is shown to behave like a unipolar diodes. When the effects of the adjacent microchannels are accounted for, the channel behaves like a diode only in a small voltage domain, while at larger voltages, the response is determined by the microchannels. The theoretical results are confirmed by numerical simulations.

I. INTRODUCTION

Permselective nanochannels have garnered much interest in the last decade due to the many applications to which they are relevant [1–3]. Their ability to filter ions based on their electric charge [4–8] has made them an ideal tractable model for permselective membranes commonly used in desalination [9,10]. Also, due to their small size, they are ideal biomolecular detectors where the molecules are detected via a change in the electrical current due to modification of the channel surface charge [11] or simply due to steric effects [12]. Of particular interest is their potential to act as fluid-based diodes [13] similar to their solid-state counterparts [14] where the nanochannel can potentially rectify the electric current by orders of magnitudes [13,15]. The diodelike behavior depends on the distribution of the surface within the channel as well as the geometry. The two simplest surface charge distributions are those that make the diodes unipolar [16,17] or bipolar [11,16,18–21] and the simplest geometries are either straight [16,17,20–22] or conical [11,13,18,19,21] nanopores.

Nanofluidic bipolar diodes are similar to their solid-state counterparts in that they are comprised of two charged regions of opposite charges which are responsible for the symmetry breaking. In contrast, unipolar diodes are comprised of two nanochannel regions, where only one of the regions is charged, while the charge of the second region has been neutralized or modified [11,17,18]. However, diodes are not the only way to rectify the current. There are many paths to current rectification even when the entire nanochannel is homogeneously charged. Permselective nanochannels can rectify the current if any symmetry in the system is broken (varying nanochannel geometry [23–25], asymmetric microchannel geometry [26], asymmetric microchannel bulk concentrations [8,25,27–31] and/or *p*H [32], ion mobilities [33]). Thus, current rectification is a robust process. Perhaps the major difference between these different rectification paths, and the

diodelike behaviors, is that the former are usually current limited for both positive and negative flows whereas bipolar diodes exhibit a limiting current only in one direction (as do diodes). The behavior of unipolar diodes will be discussed more extensively in this work where it is shown that under different circumstances, unipolar diodes respond differently—sometimes they have one limiting current and sometimes two.

The symmetry breaking is a result of the nanochannels' permselective property whereby ions of a certain charge (counterions) are transported through the channel while ions of the opposite charge (coions) are excluded [10]. As will be discussed below, the degree to which the nanochannel can filter out these ions depends on the surface charge as well as the degree of electric double layer (EDL) overlap [26,34–37]. This permselective property is best understood at its two extremes: ideal and vanishing permselectivity. In the ideal case, due to strong EDL overlap and large surface charge [37], coions are completely excluded from the channel and their transport is completely inhibited. In the vanishing case, the EDLs do not overlap and the effects of the surface charge are rather negligible, such that coion and counterion concentration distributions hardly vary under the application of an electric field [26,38]. In the vanishing permselective limit nanochannels typically behave like classical macroscopic channels and rectification is minimal. In reality, all channels exhibit an intermediate degree of permselectivity which can be termed nonideal permselectivity [39,40]. While this more general case can be treated mathematically, the end result typically requires numerical evaluation and simple analytical solutions are not attainable [39]. In contrast, consideration of the two extreme cases vastly simplifies the mathematical analysis and allows for the derivation of simple closed-form analytical solutions [25,26,37,38]. Further, the region in which the nonideal model cannot be described accurately by either of the two extremes cases is small [26,34].

Most of the aforementioned works on diodes and/or rectification factors have been either experimental and/or numerical although some theoretical consideration has been given. Thus far theoretical works have primarily modeled the rectification

————
[*]ygreen@hsph.harvard.edu

under the assumption of vanishing permselectivity [24,30–32,41], or used the more general formulation [8,21,23,29]. In the limit of ideal permselectivity, there are even fewer works: two works for bipolar diodes [16,22], and one for a unipolar diode [16]. However, in these works, the effects of the adjacent microchannels were ignored and the systems were assumed to be completely one dimensional (1D). In a recent work [25], we derived an analytical solution for the case of a bipolar diode where the two-dimensional (2D) microchannels are not neglected. There, it is shown that not only are the effects of microchannels non-negligible, they are crucial in determining the overall response. In the sole theoretical work for the unipolar diode [16], the current-voltage response (I-V) was not given by a single expression that covered the entire voltage domain response but was comprised of a number of piecewise solutions that varied for large or small and positive or negative voltages.

This work considers ion transport through a 2D ideally permselective funnel-shaped unipolar diode in two scenarios. First, we consider the case where the unipolar diode is not connected to adjacent microchannels. While this scenario is not completely realistic, it is instructive. Section II introduces the geometry (without the microchannels) and governing equations. We derive the solution for concentration and the electric potential distributions from which we find a simple and single I-V relation. The solution derivation is based on the assumption that the 2D problem can be reduced to a qausi-1D transport problem that retains much of the 2D characteristics. We present 1D and 2D results in Sec. III. We then consider the more realistic case of when the diode is connected to adjacent microchannels. It has been established that the adding of adjacent microchannels to long nanochannels is tantamount to changing the boundary conditions at that interface [25,26,38,39]. Hence, the derivation in the first scenario will also hold for the second scenario. In Sec. IV, the derivation is extended to include the effect of the microchambers where we show that the adjacent 2D microchannels play a crucial role in determining the overall response. Concluding remarks are given in Sec. V.

II. THEOERTICAL MODEL

A. Geometry

We consider a planar Cartesian 2D funnel-shaped geometry (see Fig. 1) where the height of the upper surface is given by $h(x) = h_1 + x \tan \alpha$, where the funnel angle is $\tan \alpha = (h_2 - h_1)/\Delta$, and the length of the entire channel is $\Delta = L_1 + L_2$. The model consists of a system comprising two regions. Region 1, defined by $x \in [0, L_1]$, $y \in [0, h(x)]$, is ideally permselective which corresponds to the surface charge, σ_s, determining the nanochannels' response [34]. In region 2, defined by $x \in [L_1, \Delta]$, $y \in [0, h(x)]$, the effects of the surface charge are negligible. However, ion transport in region 2 strongly depends on transport in region 1 [34]. A plane of symmetry is defined along the x axis ($y = 0$) such that only the top surface in region 1 is charged. The case $\alpha = 0$ ($h_1 = h_2$) and $L_2 = 0$ corresponds to a straight and uniformly charged nanochannel that has previously been considered in 2D [25,38,39] and 3D [26,34,42]. To simplify the analysis, we
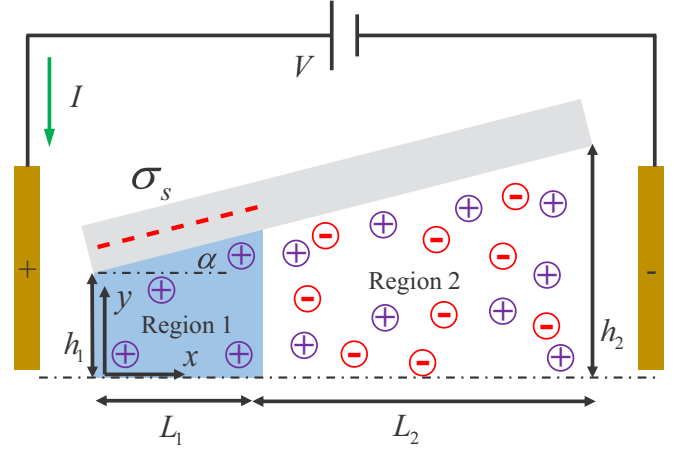

FIG. 1. Schematic of a 2D funnel-shaped channel of angle α under an applied potential V. The top surface in region 1 (marked in blue) is charged by a negative surface charge σ_s.

assume that the interface between the regions is sharp which corresponds to the soon-to-be defined parameter ε going to zero [10].

B. Governing equation

The nondimensional equations governing ion transport through a permselective medium for a symmetric and binary ($z_\pm = \pm 1$, $\tilde{D}_\pm = \tilde{D}$) electrolyte are the Poisson-Nernst-Planck (PNP) equations. In steady state and with negligible convection these are [10,35,43]

$$\nabla \cdot (\nabla c_\pm \pm c_\pm \nabla \phi) = -\nabla \cdot \boldsymbol{j}_\pm = 0, \tag{1}$$

$$2\varepsilon^2 \nabla^2 \phi = -\rho_e. \tag{2}$$

Equation (1) is the Nernst-Planck equation for continuity of ionic fluxes for the counterion, c_+, and coion, c_-, concentrations that have been normalized by the bulk concentrations $\tilde{c}_0$ (tilde denotes the parameter in dimensional form). The spatial coordinates have been normalized by the diffusion length $\tilde{L} = \tilde{L}_2$ (see Appendix A for a discussion on this normalization). The ionic fluxes are normalized by $\tilde{D}c_0/\tilde{L}$. Equation (2) is the Poisson equation for the electric potential, ϕ, which has been normalized by the thermal potential $\Re T/F$, where $\Re$ is the universal gas constant, T is the absolute temperature, and F is the Faraday constant. The nondimensional charge density, ρ_e, appearing in Eq. (2) is normalized by $zF\tilde{c}_0$. The normalized Debye layer is

$$\varepsilon = \tilde{\lambda}_D / \tilde{L}, \tag{3}$$

with

$$\tilde{\lambda}_D = \sqrt{\varepsilon_0 \varepsilon_r \Re T / (2F^2 \tilde{c}_0)}, \tag{4}$$

where ε_0 and ε_r are the permittivity of vacuum and the relative permittivity of the electrolyte, respectively. The space charge density [25,26,38,44] is

$$\rho_e = c_+ - c_- - N\delta_{1,k}, \tag{5}$$

where k represents the regions ($k = 1, 2$) and $\delta_{1,k}$ is Kronecker's delta. The average excess counterion concentration, N, in region 1 is related to the surface charge, σ_s, of the walls [26,37]. The exact $N - \sigma_s$ relation is given below.

C. Permselectivity and boundary conditions

We consider the boundary conditions (BCs) at $y = 0$ and $y = h(x)$. The ionic flux is zero

$$\boldsymbol{j}_\pm \cdot \hat{\boldsymbol{n}} = 0. \tag{6}$$

At $y = 0$, the normal is $\hat{\boldsymbol{n}} = \hat{\boldsymbol{y}}$ while at $y = h(x)$, the normal to the wall is $\hat{\boldsymbol{n}} = \{h_{,x}, -1\}/\sqrt{1 + h_{,x}^2}$ [( )$_{,x}$ denotes a spatial derivative of x]. Small angles $\tan\alpha \approx \alpha \ll 1$ imply $\hat{\boldsymbol{n}} \cong -\hat{\boldsymbol{y}}$ such that

$$\boldsymbol{j}_\pm[x, y = 0, h(x)] \cdot \hat{\boldsymbol{y}} = 0. \tag{7}$$

Since region 1 is ideally permselective, the coion flux through it is $\boldsymbol{j}_- \cdot \boldsymbol{x} = 0$. Combined with Eq. (7) this results in $\boldsymbol{j}_- \overset{\Delta}{=} 0$. However, if $\tan\alpha \sim 1$, then $\boldsymbol{j}_\pm \cdot \boldsymbol{y} \neq 0$ which would result in $\boldsymbol{j}_- \neq 0$ in the bulk. As will soon be shown, the combination of no flux at the walls, as well as $\boldsymbol{j}_- \overset{\Delta}{=} 0$, results in quasi-1D transport. Yet, the transport will still retain some of its 2D properties. Similarly, the BCs for the electric potential are

$$\phi_{,y}(x, y = 0) = 0, \quad \phi_{,y}[x, y = h(x)] = \sigma\delta_{1,k}, \tag{8}$$

where σ is the normalized surface charge [normalized by $\varepsilon_0\varepsilon_r\Re T/(F\tilde{L})$].

The analytical model will assume $\boldsymbol{j}_- \overset{\Delta}{=} 0$ and $\boldsymbol{j}_\pm \cdot \boldsymbol{y} = 0$. In the numerical simulations (see Appendix B), the boundary condition (BC) $\boldsymbol{j}_\pm \cdot \boldsymbol{n} = 0$ is enforced at $y = h(x)$ and $\boldsymbol{j}_- \overset{\Delta}{=} 0$ is not set directly [37]. Using numerical simulations, we will investigate when the $\alpha \ll 1$ assumption fails as well as investigate when the assumption of ideal permselectivity fails.

D. Solution derivation

We take the height averages of Eqs. (1) and (2), where height average quantities of $c_\pm$, ϕ are denoted by overbars and are calculated by

$$\{\bar{c}_\pm, \bar{\phi}\} = \frac{1}{h}\int_0^h \{c_\pm, \phi\}dy. \tag{9}$$

The 1D height average of Eq. (1) after accounting for the BCs discussed in Sec. II C yields

$$\bar{c}_{+,x} + \bar{c}_+\bar{\phi}_{,x} = -\bar{j}_+, \tag{10}$$

$$\bar{c}_{-,x} - \bar{c}_-\bar{\phi}_{,x} = 0, \tag{11}$$

where $j_+ = \boldsymbol{j}_+ \cdot \hat{\boldsymbol{x}} = $ const. The height averaged Poisson equation is [Eq. (2)]

$$2\varepsilon^2(\bar{\phi}_{,xx} + \sigma\delta_{1,k}/h) = -(\bar{c}_+ - \bar{c}_-). \tag{12}$$

Comparing to Eq. (5), it is easy to see that the dimensional and nondimensional excess counterion concentrations are $\tilde{N} = -\tilde{\sigma}/(F\tilde{h})$ and $N = \tilde{N}/\tilde{c}_0$, respectively. For brevity, we now shall drop the overbars.

We now make the further assumption of local electroneutrality (LEN) [10,35] where it is assumed as $\varepsilon \to 0$ (Appendix A), that $\varepsilon^2\phi_{,xx} \ll 1$. In region 2, where $\sigma \cong 0$, we have $\rho = 0$ which yields $c_{2,\pm} = c$. Then Eq. (10) yields [25,26]

$$c_{2,x} = -\frac{I}{2h(x)}, \tag{13}$$

where $\bar{j}_+ = j = I/h$. While from Eq. (11) it can be shown that [35,43]

$$\phi_2 = \ln c_2 + \hat{\phi}_{2,0}. \tag{14}$$

In region 1, while $\varepsilon \to 0$, it is assumed that $|\varepsilon^2\sigma| \gg 1$. Then, from $\rho = 0$, one has

$$c_{1,+}(x) = N_h(x) = -\frac{\sigma_s}{h(x)}, \quad c_{1,-} = 0, \tag{15}$$

where $|\sigma_s| = |2\varepsilon^2\sigma| \gg 1$. It is now apparent that the excess counterion concentration, $N = N_h = N[h(x)]$, depends on the height and varies within the channel and leads to the complete exclusion of coions from this region ($c_{1,-} = 0$). Then, the governing equation for the electric potential is

$$N_{h,x} + N_h\phi_{1,x} = -\frac{I}{h(x)}, \tag{16}$$

In both regions, we require that the total current I is conserved at each cross section. While Eqs. (13) and (16) appear to be explicitly 1D, they depend on $h(x)$, such that some of the 2D transport characteristics are retained. This will be demonstrated shortly.

The following interfacial BCs are supplemented:

$$\mu_1(0) = V, \ \mu_1(L_1) = \mu_2(L_1), \ c_2(\Delta) = 1, \ \phi_2(\Delta) = 0. \tag{17}$$

The first two terms are the requirement that the counterion electrochemical potential,

$$\mu(x) = \ln c(x) + \phi(x), \tag{18}$$

is continuous at the permselective interfaces [10,25]. At $x = \Delta$, we require the concentration to equal the bulk concentration, and the total potential drop is V. Solution of Eqs. (13), (16), and (17) yields

$$\phi_1 = V + \frac{Ix}{\sigma_s} + \ln\left[\frac{h_1(\Delta - x) + h_2 x}{-\sigma_s\Delta}\right], \tag{19}$$

$$c_2 = 1 - \frac{I}{2\alpha}\ln\left[\frac{h_1(\Delta - x) + h_2 x}{h_2\Delta}\right], \tag{20}$$

with $\hat{\phi}_{2,0} = 0$ ($\phi_2 = \ln c_2$). The current-voltage (I-V) relation is

$$V = -\frac{IL_1}{\sigma_s} + 2\ln\left(1 - \frac{I}{I_{\lim}}\right), \tag{21}$$

where the limiting current is

$$I_{\lim} = 2\alpha\left[\ln\left(\frac{h_2 L_1 + h_1 L_2}{h_2\Delta}\right)\right]^{-1}. \tag{22}$$
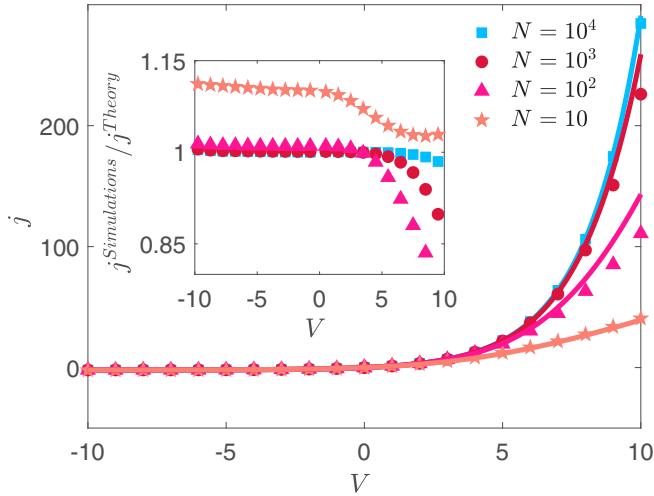
FIG. 2. 1D current density–voltage (j-V) curve for varying values of N (simulations—markers; theory—solid line). Color coding of theory corresponds to the according simulations. (Inset) Ratio of $j^{\mathrm{Simulations}}/j^{\mathrm{Theory}}$ vs V. Simulation parameters are $L_1 = L_2 = 1$, $\varepsilon = 10^{-4}$.

III. RESULTS

A. One-dimensional results

We start off by considering a 1D geometry ($\alpha = 0$). Equation (21) reduces to

$$V = jL_1/N + 2\ln(1 + jL_2/2). \quad (23)$$

Figure 2 shows j-V curves for varying N while the inset shows the ratio of the current density of simulations versus theory ($j^{\mathrm{Simulations}}/j^{\mathrm{Theory}}$). The numerical simulations are conducted in COMSOL$^{\mathrm{TM}}$ (Appendix B). For the smallest simulated value, $N = 10$, reasonable correspondence is observed with variations of 15%. As N increases so does the correspondence. The difference between simulations and theory can be attributed to two key factors. In the simulations, $\varepsilon \neq 0$. It is known that $\varepsilon \neq 0$ leads to the creation of nonlinear space charge at $x = L_1$ for $V < 0$ [35,36]. This space charge is known to increase the current above its theoretically predicted limiting value (where excess currents depend on ε [35,36]). Also, the deviation for $V > 0$ can be attributed to the fact that in simulations $j_- \overset{\Delta}{=} 0$ is not set directly; rather it is a result of $N \gg 1$ that leads to coion exclusion and enhanced selectivity. Thus, Eq. (23) overestimates the conductance of region 1. However, as N increases, region 1 behaves more like an ideal permselective region such that the correspondence deviation decreases. Further, as N increases, the range of good correspondence increases.

The rectification factor (RF) is defined as $\mathrm{RF} = |I_{V>0}/I_{V<0}|$. While negative currents, $|I_{V<0}| < |I_{\lim}| = |2/L_2|$, are bounded, positive currents $I_{V>0}$ are not so that RF is also unbounded as V increases. The exact values depend on N and already in 1D we can have a RF $\sim O(10^2)$. However, it should be noted that as N increases, it converges to the $N \to \infty$ solution when the first term in Eq. (23) is negligible such that the current is now only dependent on the geometry of region 2. As a result, in this situation, RF depends on only
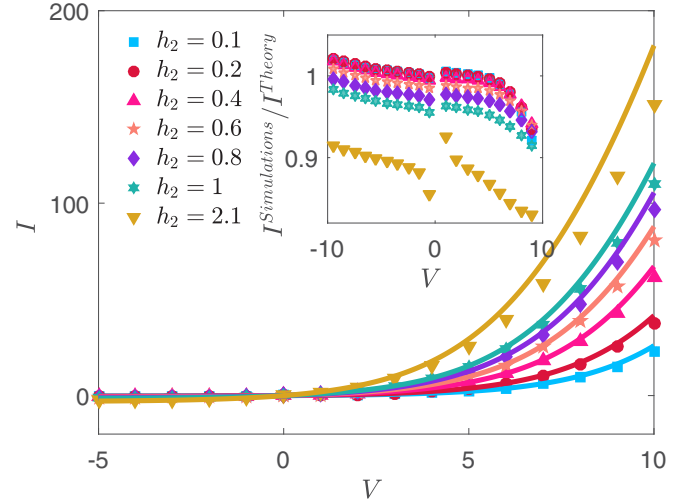

FIG. 3. Current-voltage (I-V) curves for varying values of h_2 (simulations—markers; theory—solid line). (Inset) Ratio of $I^{\mathrm{Simulations}}/I^{\mathrm{Theory}}$ vs V. Simulation parameters are $L_1 = L_2 = 1$, $h_1 = 0.1$, $N_h(h(x = 0) = h_1) = 10^3$, $\varepsilon = 10^{-3}$.

L_2. In the more general case RF depends on the 2D geometry, as well as on N and V. Given the simplicity of Eqs. (21) and (23), calculating RF for any geometry and surface charge is immediate, and it is left to the interested reader.

B. Two-dimensional results

To investigate the effect of assuming $\boldsymbol{j}_\pm \cdot \boldsymbol{y} = 0$ at $y = h(x)$ [Eq. (7)], we conducted 2D simulations where we varied the height h_2. Figure 3 compares the 2D I-V curves predicted by Eq. (21) to the simulations that have not made this oversimplifying assumption. The correspondence is striking for most values of h_2. Even for a large angle of $45°$ the deviation is only approximately 15%–20%. The inset of Fig. 3 shows the ratio of the current of the simulations versus the theory, $I^{\mathrm{Simulations}}/I^{\mathrm{Theory}}$. As can be expected, as h_2 increases, the correspondence decreases. From this, we conclude that for small angles, the solution using the assumption of quasi-1D transport holds.

IV. REALISTIC DIODE SYSTEMS—EFFECT OF MICROCHANNELS

In real systems, the funnel-shaped channel is not isolated from its environment but rather is connected to two adjacent microchannels (Fig. 4 inset). These microchannels can substantially change the characteristics of the transport. To show this, we add the microchambers to the system. In previous works, similar to here, we assumed that the transport in the permselective region was fully developed and quasi 1D [25,26,38]. This allows for solving separately in different regions and connecting the regions through a set of modified interfacial BCs. We provide the solutions for the concentration and electric potential distributions in each of these regions. Thereafter, we comment on a few issues related to these solutions. See Refs. [25,26,38,45] for a detailed derivation

and discussion. The solutions for the left and right channels (as in the inset of Fig. 4) are denoted by the subscripts L and R, respectively. The concentration and electric potential distributions are

$$c_L = 1 - \frac{I(x + L_L)}{2H_L} - I \sum_{n=1}^{\infty} \frac{\sin(\lambda_{L,n} h_1)}{h_1 H_L \lambda_{L,n}^2 \cosh(\lambda_{L,n} L_L)} \sinh[\lambda_{L,n}(x + L_L)] \cos(\lambda_{L,n} y), \quad (24)$$

$$c_R = 1 + \frac{I(\Delta + L_R - x)}{2H_R} + I \sum_{n=1}^{\infty} \frac{\sin(\lambda_{R,n} h_2)}{h_2 H_R \lambda_{R,n}^2 \cosh(\lambda_{R,n} L_R)} \sinh\left[\lambda_{R,n}(\Delta + L_R - x)\right] \cos(\lambda_{R,n} y), \quad (25)$$

with $\lambda_{i,n} = \pi n / H_i$ and $i = L, R$. The electric potentials are

$$\phi_L = \ln c_L + V, \quad \phi_R = \ln c_R. \quad (26)$$

Several brief comments are warranted. The total potential drop, V, refers to the drop across the entire system $\phi_L(-L_L, y) = V$, $\phi_R(\Delta + L_R, y) = 0$, whereas previously V was the potential drop across the diode alone. At the two ends of the systems, the bulk concentration are set by the BCs $c_L(-L_L, y) = c_R(\Delta + L_R, y) = 1$. At the three interfaces, $x = 0, L_1, \Delta$, the total current, I, is conserved. The results from Sec. II D and Eqs. (24)–(26) are connected through a modified [relative to Eq. (17)] interfacial BC,

$$\mu_L(0) = \mu_1(0), \; \mu_1(L_1) = \mu_2(L_1),$$
$$c_2(\Delta) = c_R(\Delta), \; \mu_2(\Delta) = \mu_R(\Delta), \quad (27)$$

from which we find the I-V response:

$$V_4 = -\frac{I L_1}{\sigma_s} - 2 \ln \left(\frac{1 + I/\bar{I}_{\lim, V<0}}{1 - I/\bar{I}_{\lim, V>0}} \right). \quad (28)$$
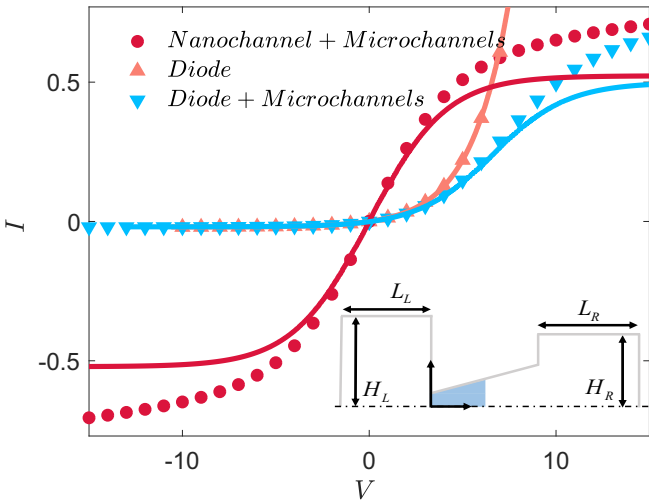

FIG. 4. Current-voltage (I-V) response curve comparing three different scenarios (simulations—markers; theory—solid line): unipolar diode without [Eq. (21)] and with [Eq. (28)] microchannels and uniformly charged nanochannel with microchannels [Eq. (32)]. (Inset) Funnel-shaped channel placed between two reservoirs: Left and Right. The height H and length L of each region are subscripted with L and R accordingly. Simulation parameters are $H_{L,R} = L_{1,2,L,R} = 1$, $h_{1,2} = 10^{-2}$, $N_h = 10^3$, $\varepsilon = 10^{-3}$.

The subscript 4 denotes the number of regions while the limiting currents are given by

$$\bar{I}_{\lim, V>0} = \left(\frac{L_L}{2H_L} + f_L \right)^{-1}, \quad (29)$$

$$\bar{I}_{\lim, V<0} = \left(\frac{L_R}{2H_R} + f_R - I_{\lim}^{-1} \right)^{-1}, \quad (30)$$

and $I_{\lim}$ is given by Eq. (22). The field focusing resistors, $f_{R,L}$, [25,26] can be attributed to the focusing of the fields from large geometries to smaller geometries. Conceptually, they are similar to the classical access resistance [46]. For the case of Cartesian geometries they are given by [25,26,38]

$$f_i = \sum_{n=1}^{\infty} \frac{\sin(\lambda_{i,n} h_i)}{h_i H_i \lambda_{i,n}^2} \tanh(\lambda_{i,n} L_i), \quad (31)$$

where h_i corresponds to the appropriate H_i for $i = L, R$. Similar expressions can be found for cylindrical pores interfacing with cylindrical microchannels [47].

It is worthwhile to compare the behavior of this less-standard four-layered system to the popular three-layer setup comprised of two microchannels connected by a nanochannel [25,26,38]. In contrast to the four-layer I-V [Eq. (28)] or even the two-layer I-V [Eq. (21)], in a three–layer setup, the assumption of $\alpha \ll 1$ results in a 1D solution that does not retain any of its 2D characteristics [25,26,38]. The I-V for the three-layer setup is

$$V_3 = -\frac{I L_1}{\sigma_s} - 2 \ln \left(\frac{1 + I/\hat{I}_{\lim, V<0}}{1 - I/\hat{I}_{\lim, V>0}} \right), \quad (32)$$

and is denoted by a subscript 3 where the limiting currents are

$$\hat{I}_{\lim, V<0} = \left(\frac{L_R}{2H_R} + f_R \right)^{-1}, \quad (33)$$

and $\hat{I}_{\lim, V>0} = \bar{I}_{\lim, V>0}$ [Eq. (29)]. For the three-layer setup ($L_2 = 0$), this requires changing the characteristic length $\tilde{L} = L_{L,R}$ (Appendix A), although this does not change any of the results discussed here. It should be noted that while Eq. (28) has yet to be verified experimentally, the predictions of Eq. (32) ($\alpha = 0$) have been verified in two separate works [34,42].

It is already evident that the both the three-layer [Eq. (32)] and four-layer [Eq. (28)] systems differ from the two-layer system [Eq. (21)]. The latter has a limiting current only for negative voltages while the former have limiting currents for both positive and negative currents. This indicates that the effects of the microchambers are of utmost importance as they eliminate the continued growth of the current discussed

in Sec. III. The positive limiting currents of the three- and four-layered systems are identical, while the negative values [Eqs. (30) and (33)] differ by the $I_{\lim}^{-1}$ term. For the case that region 2 is substantially smaller than region R, the effects can be substantial as this term will dominate the negative limiting current. As a result, the ratio of the positive and negative limiting currents can be large. Figure 4 plots the I-V curves for the three scenarios: diode and microchannels [Eq. (28)], nanochannel and microchannel [Eq. (32)], and diode without microchannels [Eq. (21)] for $\alpha = 0$ where the theoretical predictions are confirmed by numerical simulations. In contrast to what is typically reported, the microchannel scenarios exhibit both positive and negative limiting currents such that they differ from a strict diodelike behavior. Yet, in a certain range, both scenarios appear to be virtually the same. Hence, measuring the I-V for a small range of voltages, one might observe only the negative limiting, from which it would be deduced that there is no positive limiting current. We will return to this point shortly.

As evident in Fig. 4, the three-layer and four-layer responses differ also in the low current and/or voltage response. This too has additional interesting implications. To highlight this, we take a Taylor series of V_4 and V_3 for small currents $I \ll 1$. For simplicity we consider the case of $\alpha = 0$ (or $h_{1,2} = h$) and calculate the total resistance, $R = V/I$, of each system,

$$R_4 = -\frac{L_1}{\sigma_s} + \frac{L_2}{h} + R_{\text{micro}}, \tag{34}$$

$$R_3 = -\frac{L_1}{\sigma_s} + R_{\text{micro}}, \tag{35}$$

where

$$R_{\text{micro}} = \left[\frac{L_L}{H_L} + \frac{L_R}{H_R} + 2(f_L + f_R) \right] \tag{36}$$

is the sum of resistance associated with the microchannels [34]. When $N \gg 1$ (or $|\sigma_s| \gg 1$), $R_3 \approx R_{\text{micro}}$, the nanochannel is no longer the dominating resistance within the system [4,48,49], but rather the response is determined by R_{micro}. We recently suggested that the nanochannel-dominating resistance paradigm be changed to reflect this understanding [34], and since then the results have been confirmed experimentally [34,50]. In contrast to the three-layer system, in the four-layer system, the diode is comprised of two highly confined regions where one region is charged while the other is not. As result, two resistances can be associated with this region, one that depends on σ_s and one that does not. Here, the surface charge independent term dominates the response, $R_4 \approx L_2/h$. As a result, at low currents, the four-layer response almost completely overlaps with the diode-only system (Fig. 4). The eventual deviation is a result of the effect of the microchannels, which once more become the dominate resistance due to the effects of depletion at high voltages [10].

Finally, while theoretically predicted, in most diode systems the positive limiting current is not observed experimentally [3]. Rather, one observes a continued increase of the current similar to the diode-only system shown in Fig. 4. One possible reason is that the I-V are measured in a small voltage domain when the positive current has still not saturated. However, it should be noted that even in simple three-layer systems the limiting current is not always observed. In fact, observations show the current continues to increase and transitions to what is known as the overlimiting current [15,42,49]. The overlimiting current can be attributed to a process commonly known as electro-osmosis of the second kind [51], whereby the applied electric operates on its own nonlinearly induced space charge [10,35,36] at the nanochannel interface. This results in the creation of electroconvective vortices that are responsible for mixing the ions more efficiently than the diffusion limited process. The lack of an observed limiting current is not limited to single channel systems but also occurs in systems comprised of multiple nanochannels [42,49]. Another possibility for the lack of observation of a limiting current is that the experimental conditions (high bulk concentrations, etc.) are such that channels are not ideally permselective, where it is known that the limiting current is shifted to larger values and the transition voltage increases with increasing concentration [40]. From an experimental standpoint, distinction should not only be made between the various two-, three-, and four-layer scenarios discussed above but also as to what the experimental conditions are and whether they correspond to ideal or vanishing permselectivity.

V. CONCLUSIONS

The key findings of this work are as follows. We have theoretically considered the case of a unipolar funnel-shaped nanochannel which is comprised of two regions: One region is ideally permselective, while the surface charge of the second region is negligible. We derive several analytical I-V relations that depend on the geometry of the system in consideration (with and without microchannel and surface charge distribution). The I-V and resultant rectification factor depend on numerous factors, including the surface charge, the geometry, and the applied voltage. We show that the microchannels play a crucial role in determining the overall response of the system. The theoretical results are confirmed by numerical simulations. Another key result of this work is that it has been shown that the unipolar diode's behavior differs substantially from a uniformly charged nanochannel where it is shown that the noncharged nanochannel (region 2) dominates the response. We note that as long as the transport in the permselective region can be assumed to be 1D, the results of this work are easily generalizable to three-dimensional (3D) geometries, straight circular pores or conical pores. It is also likely that the method used in this work can be used to derive a complete analytical solution for a similar bipolar funnel-shaped diode.

In summary, the importance of the results in this work are twofold. Fundamentally, the physics become clearer and more transparent. Applicationwise, preliminary experiments and/or simulations are no longer needed to estimate the response of the system.

APPENDIX A: PERMSELECTIVITY

The extent to which a channel is permselective depends on the degree of EDL overlap as well as the size of the

surface charge [37]. To be ideally permselective ($\boldsymbol{j}_- \stackrel{\Delta}{=} 0$), the following two constraints must be satisfied. First, a high degree of overlap corresponds to $\tilde{\lambda}_D/\tilde{h} \gg 1$. Second, large surface charge typically corresponds to $N \gg 1$. Reference [37] suggested a more restrictive constraint, which in our notation is $N \gg \tilde{\lambda}_D^2 \tilde{h}^{-1} \tilde{L}^{-1} \gg 1$. In a long 1D nanochannel, without adjacent microchannels, where transport is fully developed, there is only one characteristic length in the system and it is natural to define $\tilde{L} = \tilde{h}$ [37], which in turn leads to $\varepsilon = \tilde{\lambda}_D/\tilde{h} \gg 1$ [Eq. (3)] and $N \gg \varepsilon^2 \gg 1$. However, the situation is much more complicated when the geometry is 2D and involves two geometries (one that is permselective and one that is not) or additional microchambers. Choosing $\tilde{L}$ is rather ambiguous.

In contrast, region 2 is not highly selective on its own since the surface charge associated with the region has been neutralized leading to $N \ll 1$. However, this region is adjacent to a permselective medium. Solving for the transport in such regions typically requires using what would appear to be the opposite assumption [10,35,36]. It is assumed that adjacent to the permselective interface there is a boundary layer, whose length is of $O(\tilde{\lambda}_D)$, which controls the response. This region is typically much smaller than the diffusion length. Here, $\tilde{L} = \tilde{L}_2$ for the two-layer setup (and under certain circumstances can be either $\tilde{L} = \tilde{L}_{L/R}$ [26]). This leads to $\varepsilon \ll 1$ [10,35,36] where $\boldsymbol{j}_- \stackrel{\Delta}{=} 0$ is enforced artificially.

These different normalizations lead to drastically different ε. Which naturally raises the question—are they mutually exclusive? The answer is unsurprisingly no. The chosen normalization allows the system to be probed or investigated differently. The $\varepsilon \gg 1$ assumption is preferable to investigate the transverse behavior of the concentration and electric potential distributions. In contrast $\varepsilon \ll 1$ is preferable to investigate the axial behavior of these distributions whereby the behavior in the transverse direction is averaged out. Here, we are interested in deriving a I-V response across an elongated system so that $\tilde{L} = \tilde{L}_2$ and we take cross-sectional averages in regions 1 and 2. To ensure consistency we enforce ideal permselectivity by requiring that $\boldsymbol{j}_- \stackrel{\Delta}{=} 0$ and $c_{1,-} = 0$. Indeed, this formulation would not differ if we replaced the nanochannel with any kind of permselective medium, such that only average properties can be considered and matter. Hence, as we have previously stated [25,26,34,38,42,45], the findings of this work are not solely limited to permselective nanochannels but can also be applied to membrane systems which show similar trends [52].

In the next Appendix, we will show that numerical simulations that model either strong overlap or use cross-sectional averages are virtually identical save that the former is computationally much more expensive.

APPENDIX B: NUMERICAL SIMULATIONS

To verify our results we solved the fully coupled PNP equations given by Eqs. (1) and (2) using the finite
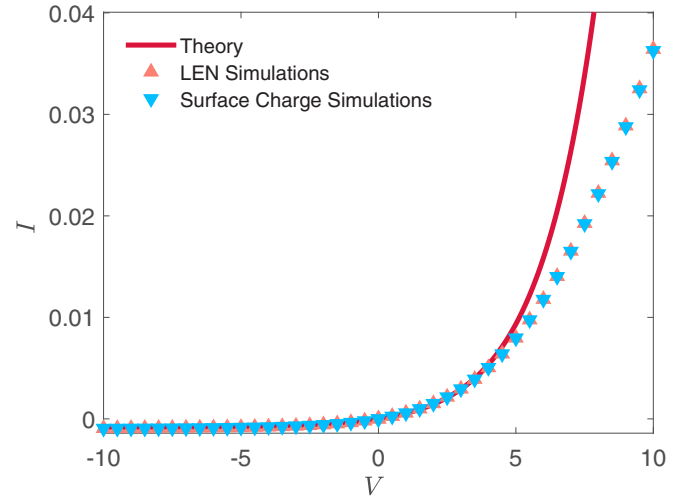

FIG. 5. Current-voltage response curve comparing the two different numerical methods for the geometry given for the following parameters: $L_1 = 0.03$, $L_2 = 1$, $h_1 = 10^{-4}$, $h_2 = 10^{-3}$, $N_h(h_1) = 150$, $\sigma_s = 7500$, $\varepsilon = 10^{-3}$.

elements program COMSOL$^{\text{TM}}$ for the two-dimensional geometry described in Fig 1. The PNP equations were solved using the Transport of Diluted Species and Electrostatic modules in COMSOL for the cases of $\varepsilon = 10^{-4}$ in 1D, and $\varepsilon = 10^{-3}$ in 2D (see our previous works for more details [25,26,34,45]).

We modeled the systems in two different ways. First, the top surface is subject to a surface charge σ_s in region 1 and the charge density $\rho_e = c_+ - c_-$ in all regions. The second method assumed that the excess counterion concentration is $N_h = -\sigma_s/h$, as described in the main text. Then, the space charge density in region 1 is given by $\rho_e = c_+ - c_- - N$. The geometry is chosen such that $h/\varepsilon = 1$ which corresponds to relatively strong overlap which will allow for comparison of these two models.

The first method requires that, at the surface, the mesh size be smaller than ε so that the behavior of the concentration within the electric double layer can be captured. This fine meshing requires approximately at least an order of magnitude more elements such that the run time approximately takes an order of magnitude longer. Further computational considerations (memory and more) constrain the geometries that are numerically solvable. This makes solving for elongated geometries virtually impossible. As such, in the main text, we used the simulations from the second model (denoted as LEN). In Fig. 5 we compare between the two models and show that they produce identical results (complete overlap). As shown in Fig. 2, correspondence between the simulations and theoretical results can be improved by increasing N (or σ_s); however, this too would result in refining the mesh at the interfaces which would further increase the run time.

[1] L. Bocquet and E. Charlaix, Nanofluidics, from bulk to interfaces, Chem. Soc. Rev. **39**, 1073 (2010).

[2] W. Sparreboom, A. van den Berg, and J. C. T. Eijkel, Principles and applications of nanofluidic transport, Nat. Nanotechnol. **4**, 713 (2009).

[3] Z. S. Siwy and S. Howorka, Engineered voltage-responsive nanopores, Chem. Soc. Rev. **39**, 1115 (2010).

[4] D. Stein, M. Kruithof, and C. Dekker, Surface-Charge-Governed Ion Transport in Nanofluidic Channels, Phys. Rev. Lett. **93**, 035901 (2004).

[5] A. Plecis, R. B. Schoch, and P. Renaud, Ionic transport phenomena in nanofluidics: experimental and theoretical study of the exclusion-enrichment effect on a chip, Nano Lett. **5**, 1147 (2005).

[6] I. Vlassiouk, S. Smirnov, and Z. Siwy, Ionic selectivity of single nanochannels, Nano Lett. **8**, 1978 (2008).

[7] A. Wolf, N. Reber, P. Y. Apel, B. E. Fischer, and R. Spohr, Electrolyte transport in charged single ion track capillaries, Nucl. Instrum. Methods Phys. Res., Sect. B **105**, 291 (1995).

[8] P. Ramírez, S. Mafé, V. M. Aguilella, and A. Alcaraz, Synthetic nanopores with fixed charges: An electrodiffusion model for ionic transport, Phys. Rev. E **68**, 011910 (2003).

[9] H.-C. Chang, G. Yossifon, and E. A. Demekhin, Nanoscale electrokinetics and microvortices: How microhydrodynamics affects nanofluidic ion flux, Annu. Rev. Fluid Mech. **44**, 401 (2012).

[10] I. Rubinstein, *Electro-Diffusion of Ions* (SIAM, Philadelphia, 1990).

[11] I. Vlassiouk, T. R. Kozel, and Z. S. Siwy, Biosensing with nanofluidic diodes, J. Am. Chem. Soc. **131**, 8211 (2009).

[12] A. Meller, L. Nivon, and D. Branton, Voltage-Driven DNA Translocations through a Nanopore, Phys. Rev. Lett. **86**, 3435 (2001).

[13] Z. Siwy, E. Heins, C. C. Harrell, P. Kohli, and C. R. Martin, Conical-nanotube ion-current rectifiers: The role of surface charge, J. Am. Chem. Soc. **126**, 10850 (2004).

[14] N. W. Ashcroft and N. D. Mermin, *Solid State Physics*, 1st ed. (Cengage Learning, New York, 1976).

[15] G. Yossifon, Y.-C. Chang, and H.-C. Chang, Rectification, Gating Voltage, and Interchannel Communication of Nanoslot Arrays due to Asymmetric Entrance Space Charge Polarization, Phys. Rev. Lett. **103**, 154502 (2009).

[16] I. Vlassiouk, S. Smirnov, and Z. Siwy, Nanofluidic ionic diodes. Comparison of analytical and numerical solutions, ACS Nano **2**, 1589 (2008).

[17] R. Karnik, C. Duan, K. Castelino, H. Daiguji, and A. Majumdar, Rectification of ionic current in a nanofluidic diode, Nano Lett. **7**, 547 (2007).

[18] I. Vlassiouk and Z. S. Siwy, Nanofluidic diode, Nano Lett. **7**, 552 (2007).

[19] D. Constantin and Z. S. Siwy, Poisson-Nernst-Planck model of ion current rectification through a nanofluidic diode, Phys. Rev. E **76**, 041202 (2007).

[20] H. Daiguji, Y. Oka, and K. Shirono, Nanofluidic diode and bipolar transistor, Nano Lett. **5**, 2274 (2005).

[21] P. Ramírez, V. Gómez, J. Cervera, B. Schiedt, and S. Mafé, Ion transport and selectivity in nanopores with spatially inhomogeneous fixed charge distributions, J. Chem. Phys. **126**, 194703 (2007).

[22] L.-J. Cheng and L. J. Guo, Ionic current rectification, breakdown, and switching in heterogeneous oxide nanofluidic devices, ACS Nano **3**, 575 (2009).

[23] P. Ramírez, P. Y. Apel, J. Cervera, and S. Mafé, Pore structure and function of synthetic nanopores with fixed charges: tip shape and rectification properties, Nanotechnology **19**, 315707 (2008).

[24] I. D. Kosińska and A. Fuliński, Asymmetric nanodiffusion, Phys. Rev. E **72**, 011201 (2005).

[25] Y. Green, Y. Edri, and G. Yossifon, Asymmetry-induced electric current rectification in permselective systems, Phys. Rev. E **92**, 033018 (2015).

[26] Y. Green, S. Shloush, and G. Yossifon, Effect of geometry on concentration polarization in realistic heterogeneous permselective systems, Phys. Rev. E **89**, 043015 (2014).

[27] L.-J. Cheng and L. J. Guo, Rectified ion transport through concentration gradient in homogeneous silica nanochannels, Nano Lett. **7**, 3165 (2007).

[28] Y. Qiu, R. A. Lucas, and Z. S. Siwy, Viscosity and conductivity tunable diode-like behavior for meso- and micropores, J. Phys. Chem. Lett. **8**, 3846 (2017).

[29] J. Cervera, B. Schiedt, R. Neumann, S. Mafé, and P. Ramírez, Ionic conduction, rectification, and selectivity in single conical nanopores, J. Chem. Phys. **124**, 104706 (2006).

[30] Z. Siwy, I. D. Kosińska, A. Fuliński, and C. R. Martin, Asymmetric Diffusion through Synthetic Nanopores, Phys. Rev. Lett. **94**, 048102 (2005).

[31] A. Fuliński, I. Kosińska, and Z. Siwy, Transport properties of nanopores in electrolyte solutions: the diffusional model and surface currents, New J. Phys. **7**, 132 (2005).

[32] A. Fuliński, I. D. Kosińska, and Z. Siwy, On the validity of continuous modelling of ion transport through nanochannels, EPL **67**, 683 (2004).

[33] T. Plett, M. L. Thai, J. Cai, I. Vlassiouk, R. M. Penner, and Z. S. Siwy, Ion transport in gel and gel–liquid systems for LiClO$_4$-doped PMMA at the meso- and nanoscales, Nanoscale **9**, 16232 (2017).

[34] Y. Green, R. Eshel, S. Park, and G. Yossifon, Interplay between nanochannel and microchannel resistances, Nano Lett. **16**, 2744 (2016).

[35] I. Rubinstein and L. Shtilman, Voltage against current curves of cation exchange membranes, J. Chem. Soc., Faraday Trans. 2 **75**, 231 (1979).

[36] E. Yariv, Asymptotic current-voltage relations for currents exceeding the diffusion limit, Phys. Rev. E **80**, 051201 (2009).

[37] O. Schnitzer and E. Yariv, Electric conductance of highly selective nanochannels, Phys. Rev. E **87**, 054301 (2013).

[38] Y. Green and G. Yossifon, Time-dependent ion transport in heterogeneous permselective systems, Phys. Rev. E **91**, 063001 (2015).

[39] R. abu-Rjal, V. Chinaryan, M. Z. Bazant, I. Rubinstein, and B. Zaltzman, Effect of concentration polarization on permselectivity, Phys. Rev. E **89**, 012302 (2014).

[40] I. Rubinstein and B. Zaltzman, Equilibrium Electroconvective Instability, Phys. Rev. Lett. **114**, 114502 (2015).

[41] I. D. Kosińska, I. Goychuk, M. Kostur, G. Schmid, and P. Hänggi, Rectification in synthetic conical nanopores: A one-dimensional Poisson-Nernst-Planck model, Phys. Rev. E **77**, 031131 (2008).

[42] Y. Green, S. Park, and G. Yossifon, Bridging the gap between an isolated nanochannel and a communicating multipore heterogeneous membrane, Phys. Rev. E **91**, 011002(R) (2015).

[43] I. Rubinstein, Electroconvection at an electrically inhomogeneous permselective interface, Phys. Fluids A **3**, 2301 (1991).

[44] J. A. Manzanares, W. D. Murphy, S. Mafe, and H. Reiss, Numerical simulation of the nonequilibrium diffuse double layer in ion-exchange membranes, J. Phys. Chem. **97**, 8524 (1993).

[45] Y. Green and G. Yossifon, Effects of three-dimensional geometric field focusing on concentration polarization in a heterogeneous permselective system, Phys. Rev. E **89**, 013024 (2014).

[46] J. E. Hall, Access resistance of a small circular pore, J. Gen. Physiol. **66**, 531 (1975).

[47] I. Rubinstein and F. Maletzki, Electroconvection at an electrically inhomogeneous permselective membrane surface, J. Chem. Soc., Faraday Trans. **87**, 2079 (1991).

[48] R. B. Schoch, H. van Lintel, and P. Renaud, Effect of the surface charge on ion transport through nanoslits, Phys. Fluids **17**, 100604 (2005).

[49] G. Yossifon, P. Mushenheim, Y.-C. Chang, and H.-C. Chang, Eliminating the limiting-current phenomenon by geometric field focusing into nanopores and nanoslots, Phys. Rev. E **81**, 046301 (2010).

[50] A. Alcaraz, M. L. López, M. Queralt-Martín, and V. M. Aguilella, Ion transport in confined geometries below the nanoscale: Access resistance dominates protein channel conductance in diluted solutions, ACS Nano **11**, 10392 (2017).

[51] S. S. Dukhin, Electrokinetic phenomena of the second kind and their applications, Ad. Colloid Interface Sci. **35**, 173 (1991).

[52] S. Sohn, I. Cho, S. Kwon, H. Lee, and S. J. Kim, Surface conduction in a microchannel, Langmuir **34**, 7916 (2018).